sustainability

Article

Influence of Heat Input on the Weldability of ASTM A131 DH36 Fillet Joints Welded by SMAW Underwater Wet Welding

Hugo Alexander Gonzalez Romero [1,2], Edinson Alfonso Bastos Blandón [3,*], Lissette Patricia Casadiego Miranda [3] and Enrique Esteban Niebles Nuñez [2,4]

[1] Ministerio de Ciencia, Tecnología e Innovación, Bogotá 111321, Colombia; hugo.gonzalez1@uac.edu.co
[2] Programa de Maestría en Ingeniería Mecánica, Facultad de Ingeniería, Universidad Autónoma del Caribe, Barranquilla 080020, Colombia; enrique.niebles@uac.edu.co
[3] Grupo de Investigación GLAMS, Escuela Naval de Suboficiales ARC, Armada Nacional de Colombia, Barranquilla 080020, Colombia; lissette.casadiego@armada.mil.com
[4] Programa de Ingeniería Mecánica, Grupo de Investigación IMTEF, Facultad de Ingeniería, Universidad Autónoma del Caribe, Barranquilla 080020, Colombia
* Correspondence: proyectosinvestigacionbc@gmail.com

Abstract: Naval vessels face multiple risks that can damage their hulls during navigation, leading to on-site repairs through the shield metal arc welding (SMAW) process and underwater wet welding (UWW). This paper presents a weldability study to identify the optimal heat input parameters to improve ASTM A131 DH36 welded joints quality, development, and sustainability. This study analyzes the influence of heat input on the microstructure and mechanical properties of underwater wet welding fillet joints welded with shield metal arc welding at 4 m water depth in a real-life environment located at the bay of Cartagena (Colombia). The methodology involves nondestructive and destructive tests, including visual inspection, fillet weld break, scanning electron microscopy (SEM), X-ray diffraction (XRD), Vickers hardness, and shear strength tests. The welds microstructure is composed of ferrite, pearlite, retained austenite, bainite, and martensite; the hardness values range from 170 HV1 to 443 HV1, and the shear strength values range from 339 MPa to 504 MPa. This indicates that high thermal inputs improve the weld quality produced by the underwater wet welding technique and can comply with the technical acceptance criteria of AWS D3.6, making them more sustainable, with less welding resources wastage and less impact on marine ecosystems.

Keywords: marine environments; on-site repairs; shipbuilding steel; SMAW; underwater welding

Citation: Gonzalez Romero, H.A.; Bastos Blandón, E.A.; Casadiego Miranda, L.P.; Niebles Nuñez, E.E. Influence of Heat Input on the Weldability of ASTM A131 DH36 Fillet Joints Welded by SMAW Underwater Wet Welding. *Sustainability* **2023**, *15*, 11222. https://doi.org/10.3390/su151411222

Academic Editors: Asterios Bakolas, Luis F.O. Silva and Kátia Martinello

Received: 29 May 2023
Revised: 28 June 2023
Accepted: 2 July 2023
Published: 19 July 2023

1. Introduction

In recent years, Colombian naval vessels have faced new challenges associated with the development of operations in support of the Colombian Scientific Expeditions in Antarctica, within the framework of the Colombian Antarctic Program (PAC—Programa Antártico Colombiano), exposing them to an inhospitable environment with a greater risk to the structural integrity of these vessels. Colombia's Antarctic Scientific Agenda 2014–2035 paved the way for the first Scientific Expedition, known as the "Caldas Expedition", carried out aboard the Colombian Navy (ARC—Armada de la República de Colombia) vessel "20 de Julio". This expedition marked a milestone in Colombian Antarctic science, materializing the country's interests in the Antarctic territory [1,2]. Recognizing the strategic importance of scientific research, the ARC, in the Naval Strategic Plan 2020–2023 (PEN—Plan Estratégico Naval), proposes the strengthening of the PAC by promoting regional projection and global cooperation [3]. This new operational scenario led to structural adaptations of this vessel for polar navigation with high-strength steels such as ASTM A131 DH36, which exhibits exceptional mechanical properties capable of withstanding the extreme conditions of this environment. Additionally, these improvements were necessary to ensure the safety of the vessel due to the risk of collision with icebergs or running aground in Antarctica [4,5].

In this direction, it became necessary to evaluate the behavior of ASTM A131 DH36 steel in underwater wet welding processes to develop possible on-site repairs of the wetted surface area of the naval vessels. The SMAW underwater wet welding process involves manually joining two metals while in direct contact with water. To ensure water resistance, waterproofed electrodes are utilized. The high temperatures generated by the arc result in the creation of a gaseous atmosphere during the fusion of the base and filler materials. This gaseous atmosphere chemically interacts with the weld metal (WM), base metal (BM), and the surrounding aquatic environment [6,7]. Underwater welding presents certain challenges, such as the dissociation of hydrogen from saline water, its diffusion into the weld metal, arc stability, and rapid cooling rates. These factors contribute to the formation of pores and cracks in both the weld metal and the heat-affected zone (HAZ), as well as the development of high hardness in the HAZ. Consequently, the mechanical resistance and toughness of the welded joint are compromised, resulting in lower levels of these properties [8]. It is crucial to assess the impact of heat input on the weldability and mechanical properties of steels welded using the UWW method. In a study conducted by Jiajing Pan et al. [9] on the weldability of E36 steel in underwater conditions, it was observed that the HAZ near the weld metal undergoes a complete transformation into lath martensite and exhibits increased hardness; in addition, Dariusz Fydrych et al. [10] described the weldability challenges of high-strength steels (HSS), such as cold cracking, and proposed an experiment to evaluate the bead tempered technique as an improvement in weldability of these steels in UWW conditions, obtaining that the bead tempered technique reduces the maximum HAZ hardness from 400 HV10 to less than 350 HV10, which demonstrates the suitability of the bead tempered technique for welded joints of HSS. Meanwhile, Zahit Çolak et al. [11] performed welded joints of ASTM A131 AH36 steel using atmospheric SMAW, UWW-SMAW with casing-isolated electrodes at 8 m depth, and E6013 and E7024 electrodes to evaluate and compare the mechanical and metallurgical properties of welded joints. The lowest tensile strength is obtained on welded joints with an E6013 electrode, and the width of the underwater welds HAZ is approximately 30% of the width of the atmospheric welds. Winarto Winarto et al. [12] performed an underwater wet SMAW process on ASTM A131 AH36 steel plates at 5 m and 10 m depth with an electric current variation of 120 A, 140 A, and 250 A. They also used rutile-based electrodes E6013 and E7024, similar to the underwater electrode E7014 (Broco UW-CS-1). Their findings include that the hardness value increases in WM, but the HAZ tends to have the highest hardness compared to the weld metal and base metal; also, the hardness values for both electrodes (E6013 and E7024) are like electrode (E7014).

Microstructural structures within the BM, HAZ, and WM significantly influence the mechanical properties of the welds. To have a better understanding of the microstructural behavior of ASTM A131 DH36 steel, Lijun Yang et al. [13] studied the microstructure and mechanical properties of local dry underwater-welded joints of ASTM A131 DH36 steel welded with the flux-cored tungsten inert gas (FCTIG) process using rutile-type and basic-type flux-cored electrodes. Their findings show that the obtained microstructures are composed of mostly acicular ferrite (AF), granular bainite (GB), and pro-eutectoid ferrite, increasing the hardness and strength of the welded joint. Also, the presence of large amounts of alloying elements in rutile-type flux-cored wire promotes the formation of acicular ferrite in the weld bead, which improves the micro-hardness and strength of the bead. Another study conducted by Weidong Zhao et al. [4] shows the fatigue crack propagation rates at room temperature and at −60 °C in butt-welded ASTM A131 DH36 steel joints, and a metallography test shows in the WM a significant amount of bainite and part martensite and retained austenite (RA); the HAZ area presents lath-like martensite (LM) and ferrite (F), and the BM shows pearlite (P) and ferrite. The Vickers hardness test shows that at −60 °C, the weld joints and the base metal present higher hardness values than those at room temperature, with higher hardness in the weld joint. Additionally, the N. Yasari et al. [14] study shows that a butt-welded SS400 steel microstructure is composed of grain boundary ferrite (GBF), ferrite with aligned second phase (FSA), AF, and polygonal ferrite (PF), explaining that with increasing heat input the size of the GBF and FSA laths increases, and during the cooling process of the WM, the GBF core at the main austenite grain boundaries at high temperature serves as a nucleation site for FSA. Hanqing Lu et al. [15], to improve fillet weld sizing criteria, conducted a study using longitudinal and transversal shear specimens with materials having a tensile strength between 490 MPa and 660 MPa and weld sizes between 3 mm and 10 mm. The test results show two significantly different results for the shear strength values but reveal that the shear strength definition correlates the fillet weld strength data of both types of specimens.

This study aims to contribute to the comprehensive understanding and improvement in the quality of fillet-welded joints in steel for naval applications. Specifically, T joints and overlapping joints were selected for their relevance in the underwater repair of naval vessels. The objective of this research paper was to investigate the influence of heat input on the weldability and mechanical behavior of fillet-welded joints in ASTM A131 DH36 steel. The joints were obtained through actual wet welding using the SMAW process in a real marine environment, specifically a tropical submarine setting. To analyze the weld soundness in T joints and evaluate the hardness and shear resistance in overlapping joints, two distinct heat inputs were applied. This parameterization was carried out during the welding stage of the fillet joints in accordance with the AWS D3.6 standard. The performance of the microstructure in the weld regions was assessed by examining the Vickers micro-hardness values. Additionally, the behavior of the joints in terms of resistance to longitudinal and transverse shear forces was discussed. This study further delves into the performance of each heat input under the established test conditions. The novelty of this work lies in addressing the pressing need to enhance the understanding and overall quality of fillet-welded joints in ASTM A131 DH36 steel when exposed to wet environments. By conducting a thorough examination of the influence of two distinct heat inputs on the weldability and mechanical properties of these joints, the study offers valuable insights for real-life scenarios involving UWW-SMAW processes. This research is a response to the evolving operational requirements of ARC naval vessels, aiming to support sustainable scientific expeditions that serve the best interests of humanity through the adoption of environmentally friendly welding practices.

2. Materials and Methods

2.1. Base Metal

The material used in this study is ASTM A131 DH36 with dimensions of 300 mm × 100 mm × 10 mm for T fillet joints, 270 mm × 75 mm × 10 mm and 200 mm × 50 mm × 6 mm for longitudinal fillet weld shear strength test specimens named RCL, and 200 mm × 150 mm × 10 mm and 115 mm x 150 mm × 6 mm for transversal fillet weld shear strength test specimens named RCT with the distribution shown in Figure 1.

2.2. Test Methods

Chemical and mechanical properties for ASTM A131 DH36 are described in Tables 1 and 2 and were obtained from ASTM A131 "Standard Specification for Structural Steel for Ships" [16]. Chemical analysis was performed by optical emission spectrometry OES according to ASTM E415 "Standard Test Method for Analysis of Carbon and Low-Alloy Steel by Spark Atomic Emission Spectrometry" [17] using a BRUKER Q8 MA-GELLAN spectrometer.

Table 1. Chemical composition for ASTM A131 DH36 higher-strength structural steel, in wt%.

ASTM A131 DH36 Chemical Composition Requirements													
C	**Mn**	**Si**	**P**	**S**	**Al**	**Nb**	**V**	**Ti**	**Cu**	**Cr**	**Ni**	**Mo**	**Ca**
0.18	0.90 1.60	0.10 0.50	0.035	0.035	0.015	0.02 0.05	0.05 0.10	0.02	0.35	0.20	0.40	0.08	0.005

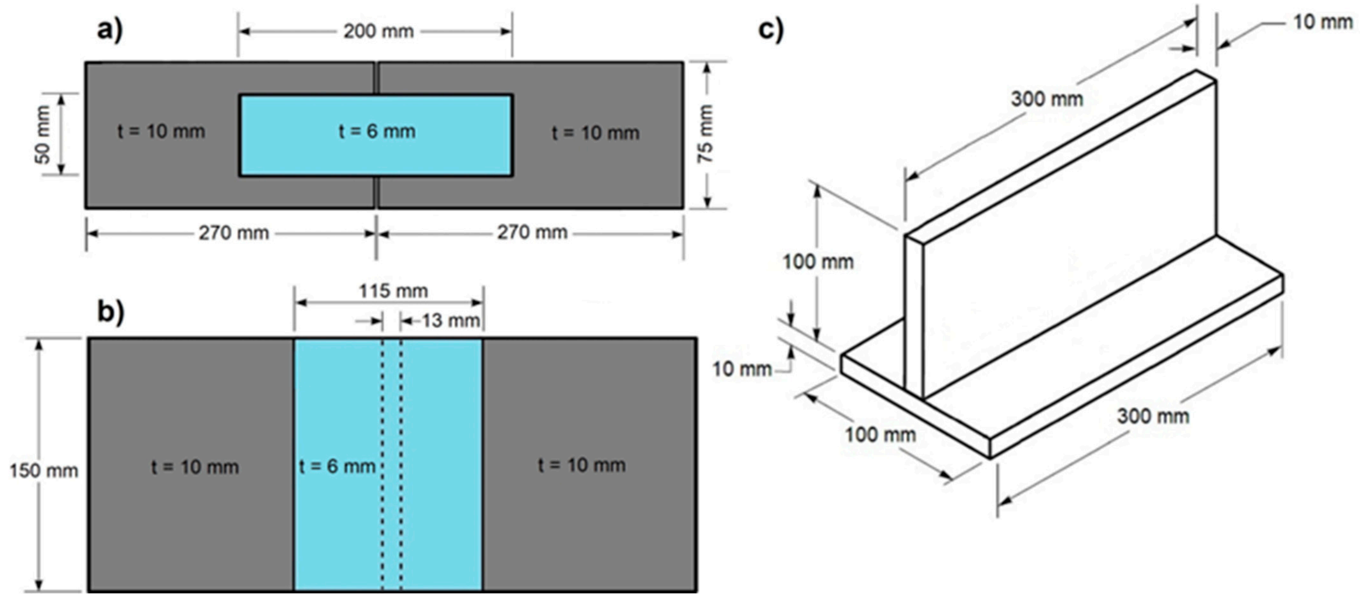

Figure 1. Steel plates distribution. (**a**) Longitudinal fillet weld shear strength test plates. (**b**) Transversal fillet weld shear strength test plates. (**c**) Fillet weld break test plates.

Table 2. Tensile and Ceq requirements for ASTM A131 DH36 higher-strength structural steel.

Grade	UTS [MPa]	YS [MPa]	Thickness [mm]	E (50 mm) [%]	C_{eq} [%]
DH36	490 to 620	355 min.	5.0–10	20 min.	0.38

Tensile test was conducted following ASTM E8 "Standard Test Methods for Tension Testing of Metallic Materials" [18], using a tensile testing machine UNITED TESTING SHFM-600kN, and ultimate tensile strength (UTS) was evaluated using method 7.10 at 10 mm/min crosshead testing speed. Yield strength (YS) was assessed using method 7.7.3 at 1 mm/min crosshead testing speed and elongation (E) after fracture was evaluated with method 7.11.2 with a gauge length of 50 mm.

Carbon equivalent Ceq was determined from de Spark OES analysis using the carbon equivalent formula described in ASTM A131 (8.2.4) [16].

$$\text{Ceq } (\%) = C + Mn/6 + Cr/5 + Mo/5 + V/5 + Ni/15 + Cu/15 \quad (1)$$

Vickers hardness (HV) tests were executed in the base metal and weld joints as per AWS D3.6:2017 "Underwater Welding Code" [19], AWS B4.0 "Standard Methods for the Mechanical Testing of Welds" [20], and ASTM E384 "Standard Test Method for Microindentation Hardness of Materials" [21], using a hardness testing machine STRUERS DuraScan G4 and a Vickers indenter applying a maximum test force of 9.8 N for 10 s and separation of indentations of minimum 500 microns.

The microstructures of the base metal and weld joints were obtained by grinding and polishing the specimens following ASTM E3 "Standard Guide for Preparation of Metallographic Specimens" [22] and microetching the specimens with 2% Nital etchant for 10 s in compliance with ASTM E407 "Standard Practice for Microetching Metals and Alloys" [23]. Microstructure images were obtained using optical microscopy (OM) using a NIKON MA100N microscope and scanning electron microscopy (SEM) using a JEOL JSM-6490 microscope. Also, microstructural analysis was confirmed by X-ray diffraction (XRD) of 3 specimens using a PANalytical X-ray diffractometer with a Co source, wavelength $K\alpha1(A) = 1.78901$, $K\alpha2(A) = 1.79290$, a continuous mode radiation scan over a 2θ diffraction fringe (35.0131°–152.4551°), 0.0260° step size, 30 mA, and 40 kV.

Fillet weld break and macroetch tests were realized according to AWS D3.6M [19] requirements established in its sections 7.10.2 and 7.10.7 (Figure 2a). The test specimens were visually examined in their entire length, the fillet break test specimens were cut of 150 mm and were loaded with a tensile test machine in compression mode located in a way that the root of the weld is exposed to tensile stress until the specimen breaks. Macroetch specimens were cut of 75 mm, and a clear definition of the base metal, heat-affected zone, and weld metal were obtained by the macroetch test, performed according to the AWS D3.6M (7.10.2) by cutting the cross-section of the weld test specimen and etching according to ASTM E340 "Standard Practice for Macroetching Metals and Alloys" [24].

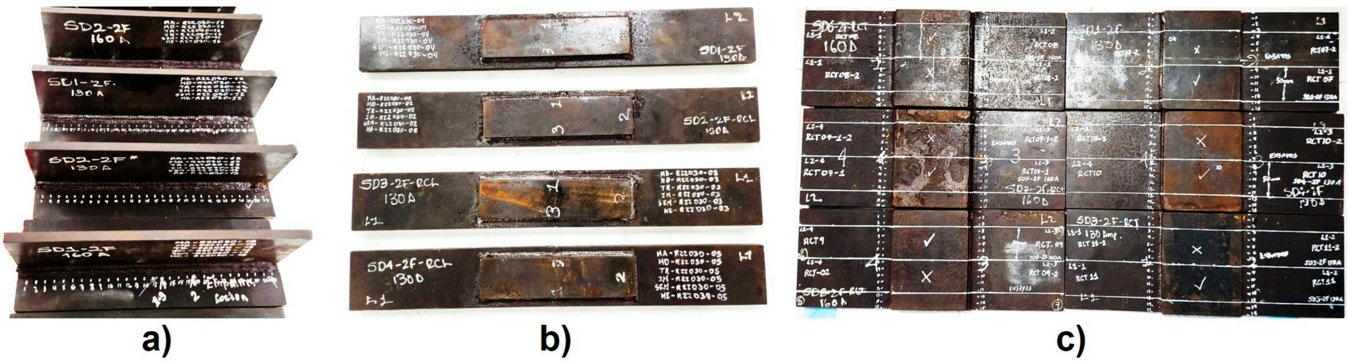

Figure 2. (**a**) Fillet T joints, (**b**) longitudinal fillet weld shear strength test, and (**c**) transversal fillet weld shear strength test welded specimens.

Longitudinal (RCL) and transversal (RCT) fillet weld shear strength test specimens were prepared for longitudinal and transversal fillet weld shear strength following section 7.10.8 of AWS D3.6M (Figure 2b,c). The average throat and length of test weld were measured before testing, the cross-sectional area was calculated by multiplying the weld length by the average throat. Finally, the specimens were ruptured under a tensile load applied by a tensile testing machine UNITED TESTING SHFM-600kN, the maximum load was registered, and the shear strength was calculated by dividing the maximum load reported by the cross-sectional area.

2.3. Manufacture of Underwater Wet Welding Welded Fillet Joints

2.3.1. Welding Equipment and Welders

UWW fillet joints were made in the ARC's Bolivar naval base in The Department of Diving and Salvage's dock with an underwater welding machine operated by underwater welders certified as professional divers who are part of the Department of Diving and Salvage's crew using the underwater welding equipment (Figure 3) composed of a Kirby Morgan diving helmet, a semi-autonomous diving suit, a 90 m long positive buoyancy umbilical cord, a Control box AMRON INTERNATIONAL AMCOMMAND II, a compressor ACFM QUINCY 5120, surface monitoring equipment OUTLAND TECHNOLOGY, a LINCOLN ELECTRIC AIR VANTAGE 500, and for this specific purpose a SofTouch® Mild Steel Underwater Welding Electrode E7014 of 1/8" (3.18 mm).

2.3.2. Welding Process Parameters for UWW Fillet Joints

The SMAW process was utilized to fabricate fillet T joints and longitudinal shear strength (RCL) and transversal shear strength (RCT) fillet weld test specimens. The welding process was carried out under 4 m of water depth, weak to moderate ocean current, and good visibility, using average welding parameters outlined in Table 3. The primary objective was to apply 2 distinct heat inputs, controlled mainly by applied currents of approximately 130 A and 160 A, to produce heat inputs ranging between 0.9 kJ/mm and 1.5 kJ/mm. Heat inputs were obtained by applying welding parameters acquired through preliminary tests using previous studies conducted by Gao Wenbin et al. [25] and Tomków Jacek et al. [26,27]

as guiding documents. The chosen welding parameters aimed to achieve both low and high heat inputs by adjusting only the applied current, to facilitate the fabrication of underwater wet-welded ASTM A131 DH36 fillet T joints, longitudinal shear strength fillet weld test specimens, and transverse shear strength fillet weld test specimens.

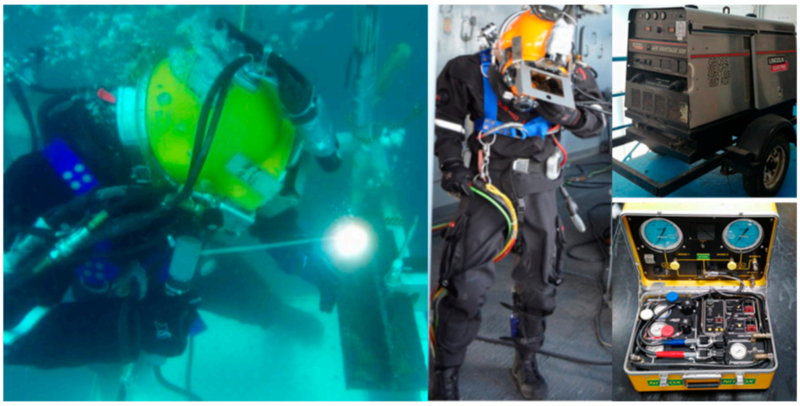

Figure 3. Underwater wet welding of fillet T test specimen and underwater welding equipment.

Table 3. Welding process parameters for fillet T joint, RCL, and RCT test specimens.

ASTM A131 DH36 Welding Parameters					
Test Plate	**Specimen ID**	**Welding Speed (mm/s)**	**Welding Voltage (V)**	**Welding Current (A)**	**Energy Input (kJ/mm)**
Fillet T	SD(A)-2F-130A	4.1	32.7	127.2	1.0
	SD(A)-2F-160A	3.9	37.4	157.2	1.5
Longitudinal shear strength test (RCL)	SD(A)-2F-130A	3.7	30.0	128.3	1.0
	SD(A)-2F-160A	3.9	34.0	158.1	1.4
Transversal shear strength test (RCT)	SD(A)-2F-130A	4.5	31.5	127.5	0.9
	SD(A)-2F-160A	4.1	35.4	157.7	1.4

Fillet T joints were fabricated using a multi-pass weld, applying three weld beads on 10 mm thick plates (Figures 1c and 2a). Meanwhile, longitudinal shear strength (RCL) and transverse shear strength (RCT) fillet weld test specimens were fabricated using a single-pass weld (Figures 1a,b and 2b,c). These joint configurations were selected based on the actual procedures used for navy vessel repairs, due to the use of a 6 mm plate over the 10 mm plate.

3. Results

3.1. Characterization of Base Metal

Table 4 displays the outcomes of the chemical composition tests on ASTM A131 DH36 steel of 6 mm and 10 mm thicknesses. As per the results, the examined material does not conform to the values stipulated in ASTM A131 for aluminum and vanadium elements. Nonetheless, it is noteworthy that numeral 7.2.2 of the ASTM Standard specifies that "When vanadium and aluminum are used in combination, minimum vanadium content of 0.030% and minimum acid-soluble aluminum content of 0.010%, or minimum the total aluminum content of 0.015%." Hence, regarding chemical composition, the material complies with the requirements of the standard ASTM A131, "Standard Specification for Structural Steel for Ships" [16].

Table 5 presents the ASTM A131 requirements; the tensile test results for the ultimate tensile strength (UTS), yield strength (YS), and elongation in a 50 mm gauge length (E); and the outcome of the carbon equivalent calculation result conducted. The tensile test results show that the material meets the stipulated requirements in Table 2 by 10% for ultimate tensile strength, 12% for yield strength, and 48% for elongation in a 50 mm gauge length.

However, it should be noted that the carbon equivalent content exceeds the maximum limit established in ASTM A131. However, preliminary UWW tests conducted during the fabrication of the welded joints demonstrate that the material can be welded without compromising its performance. Also, ARC has authorized this material, which possesses higher carbon equivalent content, because it is presently the material of choice utilized in all their ships dedicated to scientific expeditions.

Table 4. Chemical composition for 10 mm and 6 mm ASTM A131 DH36 steel plates, in wt%.

ASTM A131 DH36 Requirements													
C	**Mn**	**Si**	**P**	**S**	**Al**	**Nb**	**V**	**Ti**	**Cu**	**Cr**	**Ni**	**Mo**	**Ca**
0.18	0.90 1.60	0.10 0.50	0.035	0.035	0.015	0.02 0.05	0.05 0.10	0.02	0.35	0.20	0.40	0.08	0.005
ASTM A131 DH36 (6 mm) Spark OES Analysis													
C	**Mn**	**Si**	**P**	**S**	**Al**	**Nb**	**V**	**Ti**	**Cu**	**Cr**	**Ni**	**Mo**	**Ca**
0.13	1.4	0.3	0.01	0.003	0.036	0.04	0.004	0.007	0.18	0.13	0.09	0.06	0.002
ASTM A131 DH36 (10 mm) Spark OES Analysis													
C	**Mn**	**Si**	**P**	**S**	**Al**	**Nb**	**V**	**Ti**	**Cu**	**Cr**	**Ni**	**Mo**	**Ca**
0.13	1.4	0.3	0.01	0.002	0.034	0.03	0.004	0.003	0.19	0.08	0.07	0.04	0.002

Table 5. Tensile and Ceq test results for ASTM A131 DH36 higher-strength structural steel.

Material	UTS (MPa)	YS (MPa)	Thickness (mm)	E-50 mm (%)	C_{eq} (%)
ASTM A131 DH36 Standard [9]	490 to 620	355 min	5.0–10	20 min	0.38
ASTM A131 DH36	547	402	6–10	41	0.40

The hardness tests for each transversal, longitudinal, and normal steel direction were measured at five points uniformly distributed across the area. The test results shown in Table 6 indicate an average Vickers hardness of 159 HV 1 with a calculated variation coefficient of approximately 3%, suggesting a minimal difference between the steel transversal, longitudinal, and normal directions. These outcomes are consistent with the results obtained in prior studies conducted by Bechetti Daniel et al. [28] and Gao Wenbin et al. [29].

Table 6. Base metal hardness tests.

Base metal hardness test (HV1)														
Transversal					**Longitudinal**					**Normal**				
1	**2**	**3**	**4**	**5**	**6**	**7**	**8**	**9**	**10**	**11**	**12**	**13**	**14**	**15**
161	165	168	164	154	159	161	160	159	154	154	154	160	156	151

The microstructure obtained from optical microscopy (OM) and scanning electron microscopy (SEM) for ASTM A131 DH36 steel is presented in Figure 4. The OM findings display white-etched equiaxed ferrite and dark-etched pearlite colonies. At the same time, the SEM results confirm a well-defined carbon-free equiaxed ferrite (white-etched) and a mixture of regular geometric distribution of inter-laminar cementite lamellae and ferrite that corresponds to pearlite. The ImageJ software V1.51 [30] was employed to analyze a 500x OM micrograph and determine the quantity of ferrite and pearlite in three samples. The analysis yielded an average distribution of 69.8% of ferrite and 30.2% of pearlite with a variation coefficient of 4%. These test results indicate that the distribution of ferrite and pearlite between the steel transversal, longitudinal, and normal directions are uniform and indicate a minimal difference between them. They also are consistent with the hardness test results shown in Table 6 and those obtained in prior studies conducted by Zambrano O.A. et al. [31] and Queiros Growene et al. [32].

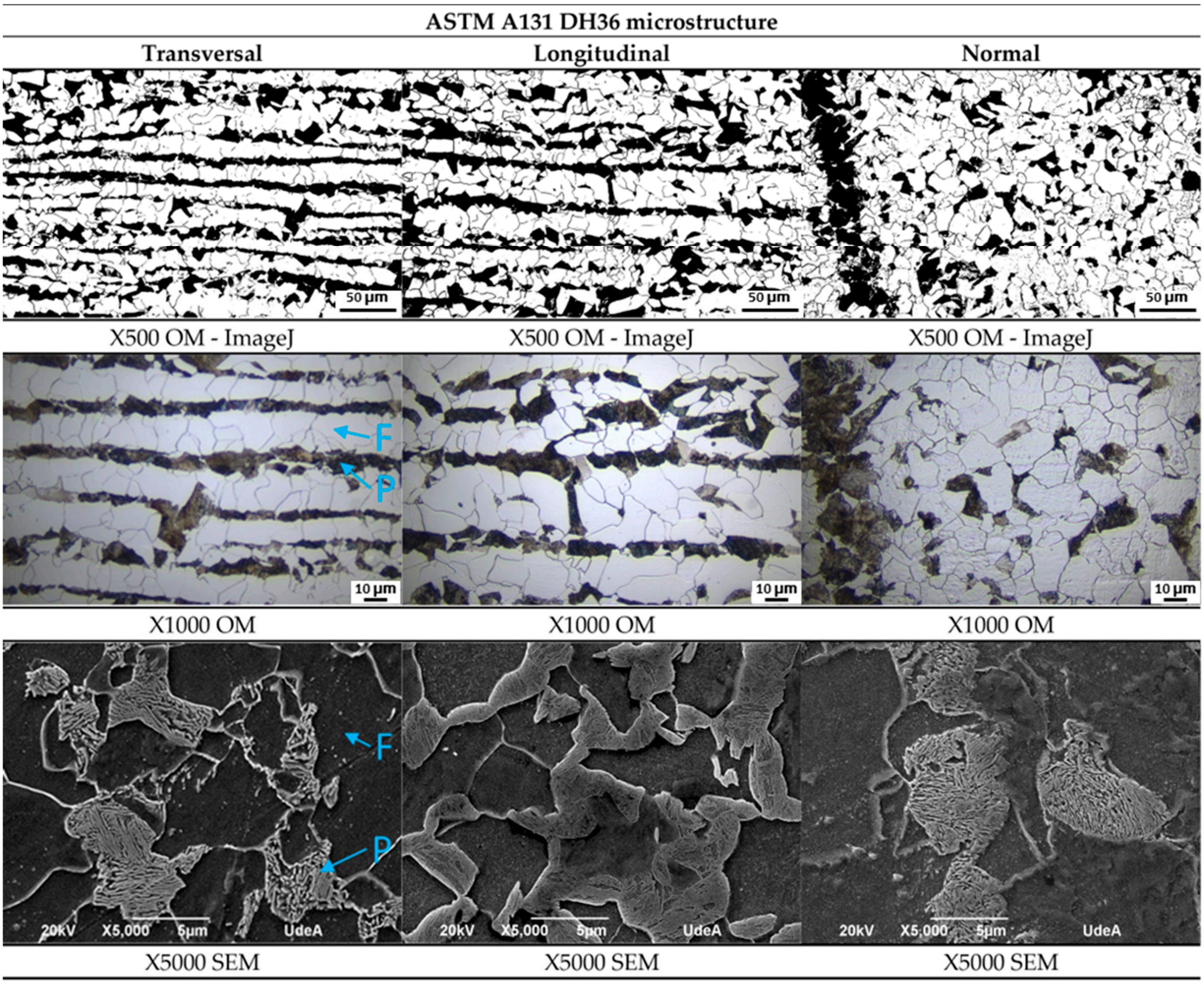

Figure 4. ASTM A131 DH36 microstructure obtained by OM and SEM.

3.2. Characterization of UWW Fillet Joints

The results of the fillet break tests of the fillet T SD(A)-2F-130A and fillet T SD(A)-2F-160A specimens are presented in Figure 5, revealing specimens with incomplete penetration (IP), lack of fusion (LF), and slag inclusions (SI) that are not acceptable for class A and B welds, according to AWS D3.6 [10] and the previous studies conducted by Civjan S.A. et al. [33] and Amirafshari P. et al. [34]. However, the welds conform to the ARC requirements for this research work and the welder's experience.

The results of the macroetch test conducted on UWW fillet-welded joints are presented in Figure 6, illustrating the base metal, heat-affected zone, and weld metal of the joints. The test results confirm IP in the fillet T and transversal shear strength specimens welded with low heat inputs. However, welded joints with higher heat inputs reveal complete fusion for the RCL, RCT, and fillet T welds specimens, indicating that the IP on fillet T welds is not present in the full length of the weld. The higher heat input welds meet the requirements of AWS D3.6 [19], and the test results are like studies conducted by Santos V.R. et al. [35] and Mohammadi S.B. et al. [36].

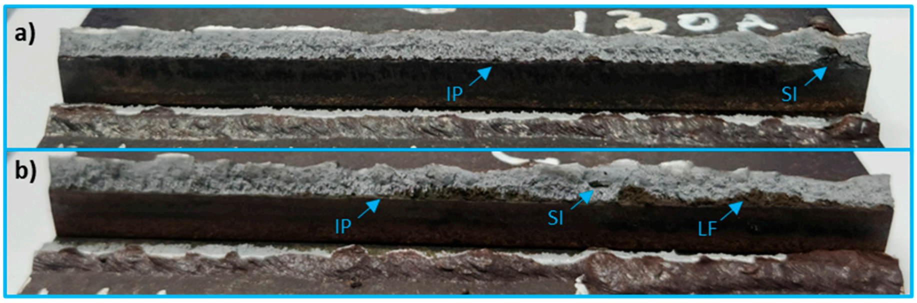

Figure 5. Fillet break test specimens for (**a**) 130 A—1.0 (kJ/mm) and (**b**) 160A—1.5 (kJ/mm).

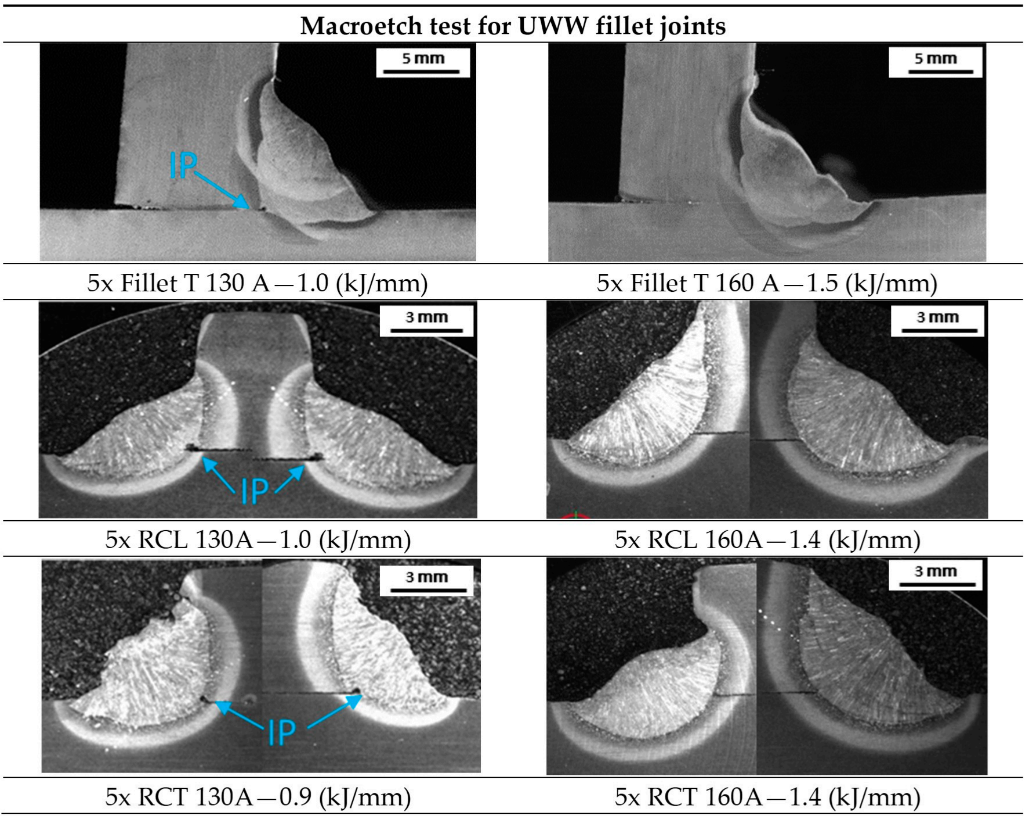

Figure 6. Macroetch of fillet T, longitudinal (RCL), and transversal (RCT) shear strength specimens.

The microstructures obtained from OM for fillet-welded joints of ASTM A131 DH36 are presented in Figure 7. The results of the OM examination indicate the presence of primary ferrite and pearlite in all base metal microstructures. This suggests that there are no significant changes in the base metal near the fillet-welded joints concerning the base metal analyzed in Section 3.1 (Figure 4) as well as the OM test results reported by Surojo Eko et al. [7] and Gao Wenbin et al. [25] where steels with similar chemical composition were analyzed. The microstructures of the fillet T HAZ display a marked difference between low and high heat inputs. At 1.0 kJ/mm (Figure 7b), the microstructure is composed of polygonal ferrite (PF), upper bainite (UB), and retained austenite (RA), which resembles the results of prior studies on similar materials by Gao Wenbin et al. [25], Toumpis Athanasios et al. [37], and Macias Fernando et al. [38]. In contrast, at 1.5 kJ/mm (Figure 7e), the microstructure displays polygonal ferrite (PF) and lath-tempered martensite (LTM), which suggests that the high heat input and multiple welded beads temper the lath martensite (LM). This finding is in line with the results reported by Macias Fernando et al. [38], Meng Fanxia et al. [39], and Zhang Hongmei et al. [40] on similar materials.

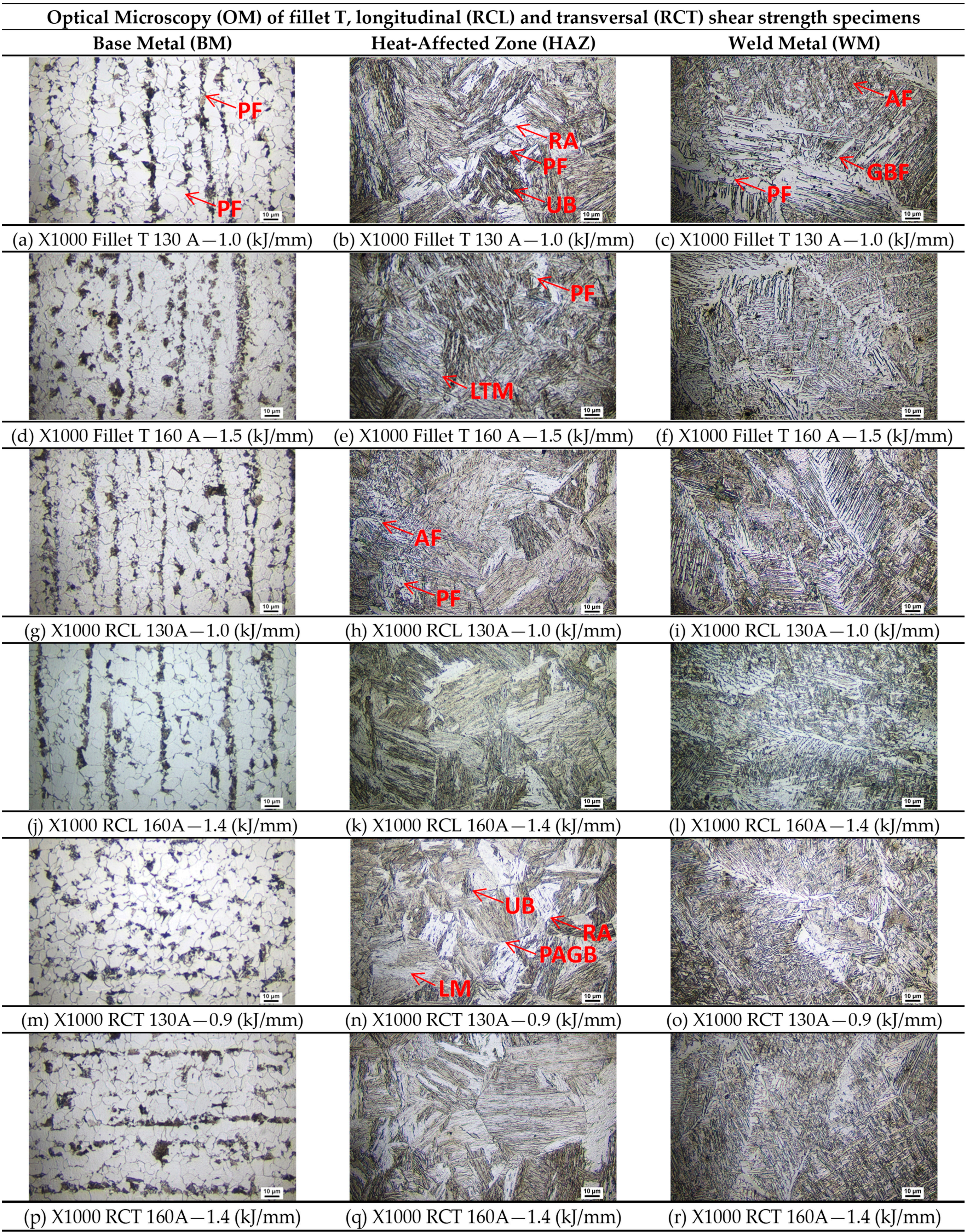

Figure 7. OM of fillet T, longitudinal (RCL), and transversal (RCT) shear strength specimens.

The microstructures of the RCL HAZ display similar results between low and high heat inputs. At 1.0 kJ/mm (h), the microstructure is composed of LM, PF, acicular ferrite (AF), and UB; at 1.4 kJ/mm (k), the microstructure displays LM and PF. The microstructures of the RCT HAZ display similar results between low and high heat inputs. At 0.9 kJ/mm (n), the microstructure is composed of LM, UB, and RA and prior austenite grain boundaries (PAGB) can be seen; at 1.4 kJ/mm (q), the microstructure displays LM, RA, and PAGB. The microstructures of the fillet T, RCL, and RCT weld metal display similar results between low and high heat inputs. The microstructures of WM for low and high heat inputs are composed of grain boundary ferrite (GBF), AF, and PF. These microstructures resemble the results of prior studies on similar materials by Gao Wenbin et al. [25], Gao Wenbin et al. [29], Toumpis Athanasios et al. [37], Li Hongliang et al. [41], Di Xinjie et al. [42], Macias Fernando et al. [38], and Kozlowska Aleksandra et al. [43].

Figure 8 presents the XRD diffractogram of the low heat input sample taken in the HAZ which reveals the presence of ferrite (PF) with orientations of (110) and (220), RA with orientations (200) and (220), as well as ferrite (310) and cementite (Fe_3C). Similarly, the XRD diffractogram of the high heat input sample taken in the HAZ shows the presence of ferrite with orientations (110) and (220), retained austenite with orientations (200) and (220), and martensite (101). Ferrite (310) and cementite (Fe_3C) are also detected. These test results confirm several structures identified by OM. They are similar to the findings of prior studies on similar materials by Jia N. et al. [44] and Medina G. et al. [45].

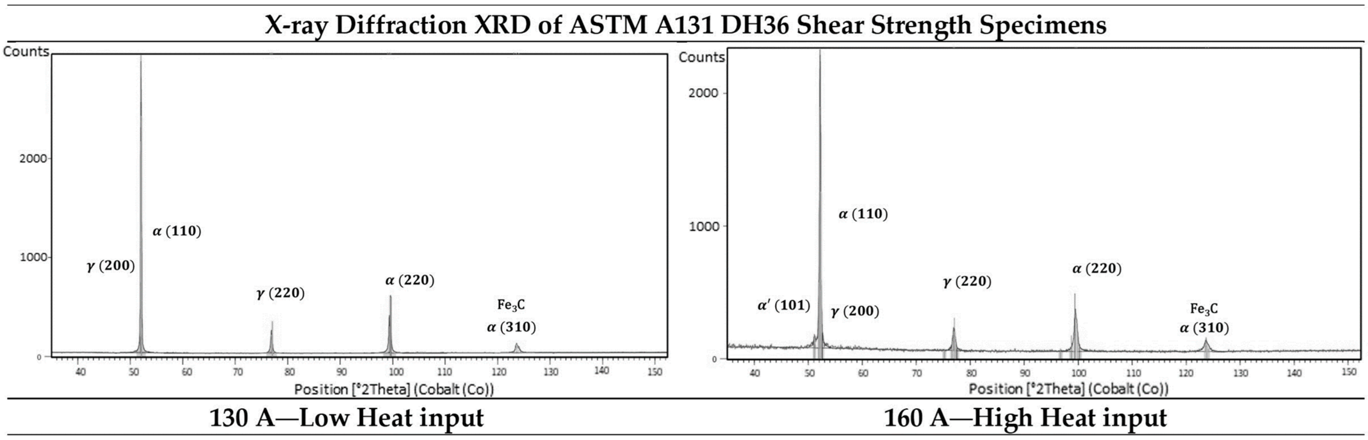

Figure 8. XRD Patterns for ASTM A131 DH36 XRD joints of low and high heat inputs.

SEM microstructures at X5000 for low and high heat input fillet welds are displayed in Figure 9. These microstructures confirm the OM findings. The (Figure 9a,d) images show the presence of carbon-free equiaxed ferrite and pearlite. The microstructure in (Figure 9b,e) presents LM, AF, UB, and PAGB for the HAZ. On the other hand, WM microstructures are composed of RA, AF, and PF with inclusions enriched with Si and Mn, suggesting the presence of inclusions such as SiO_2 and MnO because Si and Mn can easily combine with the oxygen liberated during the reaction of water with the welding heat input to form oxides. These results are similar to the findings of Gao Wenbin et al. [25].

Figure 10 presents an example of the distribution of eighteen hardness measurements taken on the welded joints according to AWS B4.0, with four measurements on the base metal, two on the weld metal, and twelve on the heat-affected zone (HAZ). Figure 11 displays the hardness profiles for all welded joints, with blue graphs indicating the fillet T joints, green graphs representing RCL joints, and red graphs depicting RCT joints. Darker colors indicate high heat inputs, while lighter colors indicate low heat inputs. All the welded joints exhibit similar behavior, with the base metal showing the lowest hardness values, the heat-affected zone displaying the highest hardness values, and the weld metal demonstrating intermediate hardness values.

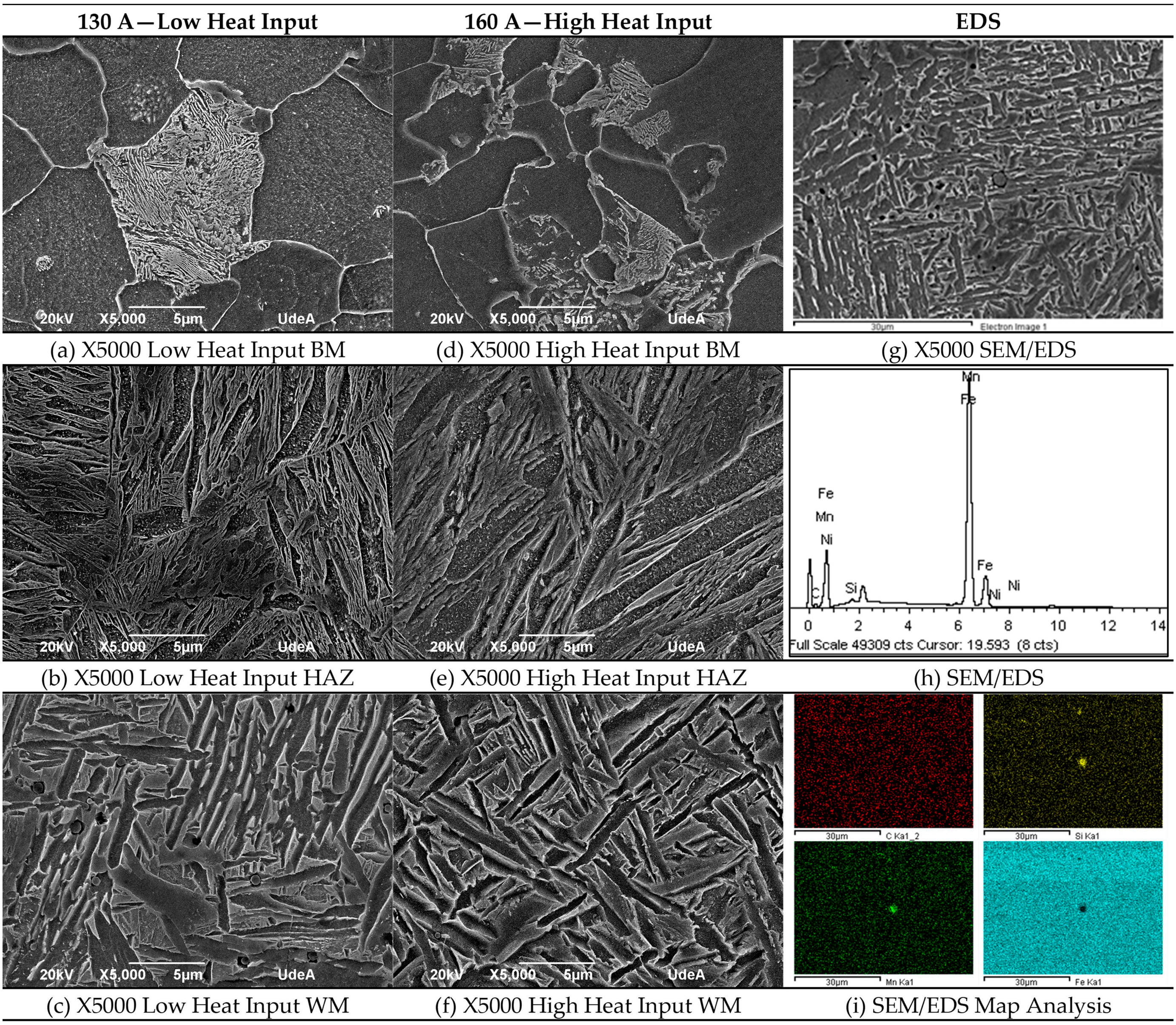

Figure 9. SEM/EDS of fillet T, longitudinal (RCL), and transversal (RCT) shear strength specimens.

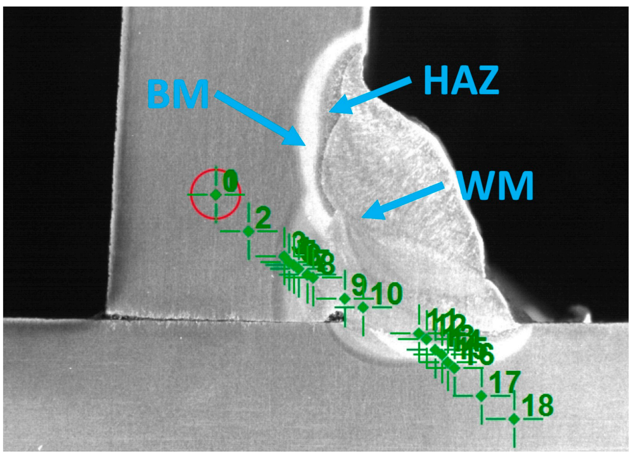

Figure 10. Example of hardness measurement's locations on the welded joints.

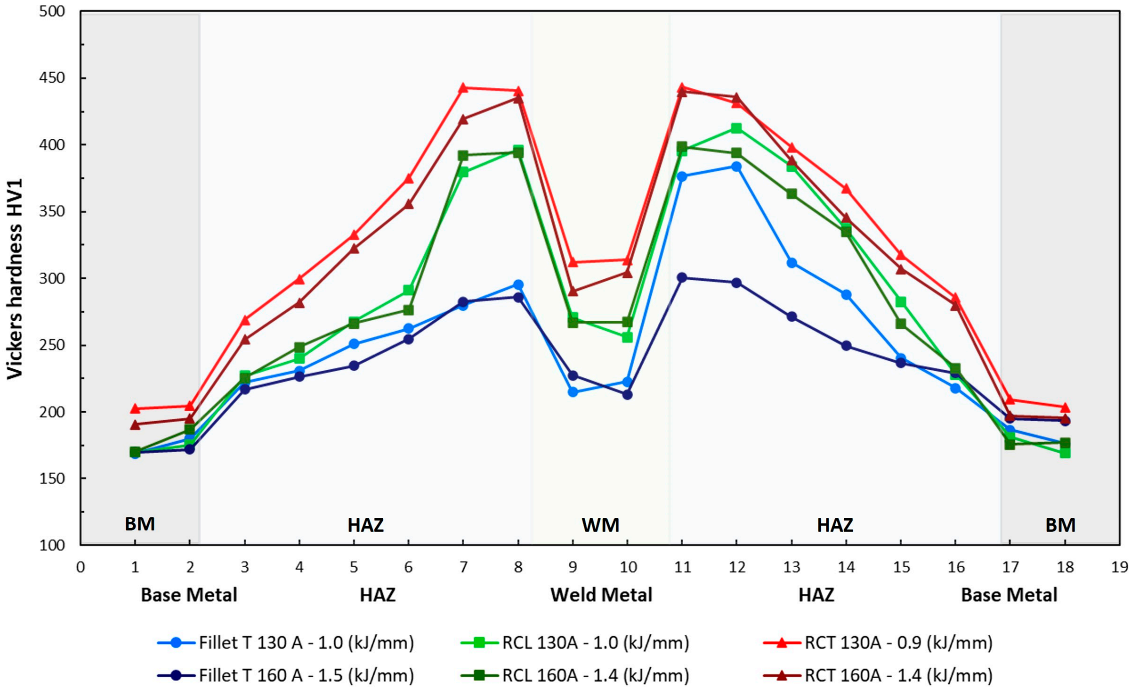

Figure 11. Fillet T, longitudinal (RCL), and transversal (RCT) shear strength, hardness profiles.

While the RCL and RTC weld profiles are similar, the RCT profiles exhibit slightly higher hardness, because the RCT joints experienced a faster cooldown rate after the welding process, likely due to the use of a single-pass weld for both joints and the RCT test specimens having a larger area in contact with the water, resulting in a higher cooldown rate for the RCT-welded joint. However, the hardness profiles of the T fillet joints exhibit different behavior compared to the RCL and RCT joints, which is attributed to the use of multiple weld passes (Figure 6). The second and third weld passes cause the welded joint experiment heat treatment that reduces the joint hardness, explaining the low values obtained for the fillet T joints. The variation in hardness values between the left and right sides of the T joint specimen 130A graph can be attributed to the positioning of the third weld pass in relation to the second one. Figure 5 illustrates that the third weld pass is situated at a distance from the HAZ created by the second pass. Consequently, the third weld pass does not impact the HAZ of the second pass, resulting in an elevated hardness level on the right side of the graph. The observed hardness behavior is consistent with prior studies on similar materials conducted by Kalyankar V.D. et al. [46] and Zhao Weidong et al. [47].

The average weld throat, weld length, area, and maximum force of the longitudinal (RCL) and transverse (RCT) specimens were measured to obtain the test results for the fillet weld shear strength. The measurements for RCL 130A are 3.35 mm, 201.60 mm, 675.26 mm^2, and 316,416.67 N, respectively, while for RCL 160A, the measures are 3.53 mm, 198.92 mm, 701.68 mm^2, and 352,752.67 N. For RCT 130A, the measurements are 3.25 mm, 200.33 mm, 651.47 mm^2, and 219,888.33 N correspondingly; for RCT 160A, the measures are 3.62 mm, 200.71 mm, 727.58 mm^2, and 257,637.33 N. These measurements were utilized to determine the shear strength of the fillet welds displayed in Figure 12. Furthermore, it is worth noting that the shear strength of RCL welds is approximately 28.74% higher than that of RCT welds. This disparity can be attributed primarily to the positioning of the tensile force during the shear strength test. In the longitudinal shear test for RCL welds, the tensile force is applied parallel to the welding bead being tested, resulting in a more favorable load distribution and higher shear strength. Conversely, in the transversal shear test for RCT welds, the tensile force is positioned transversely to the welded bead, causing weld defects to act as stress concentrators and leading to a reduction in shear strength.

Finally, the high heat inputs' shear strengths are about 5.6% higher than the low heat inputs' shear strengths.

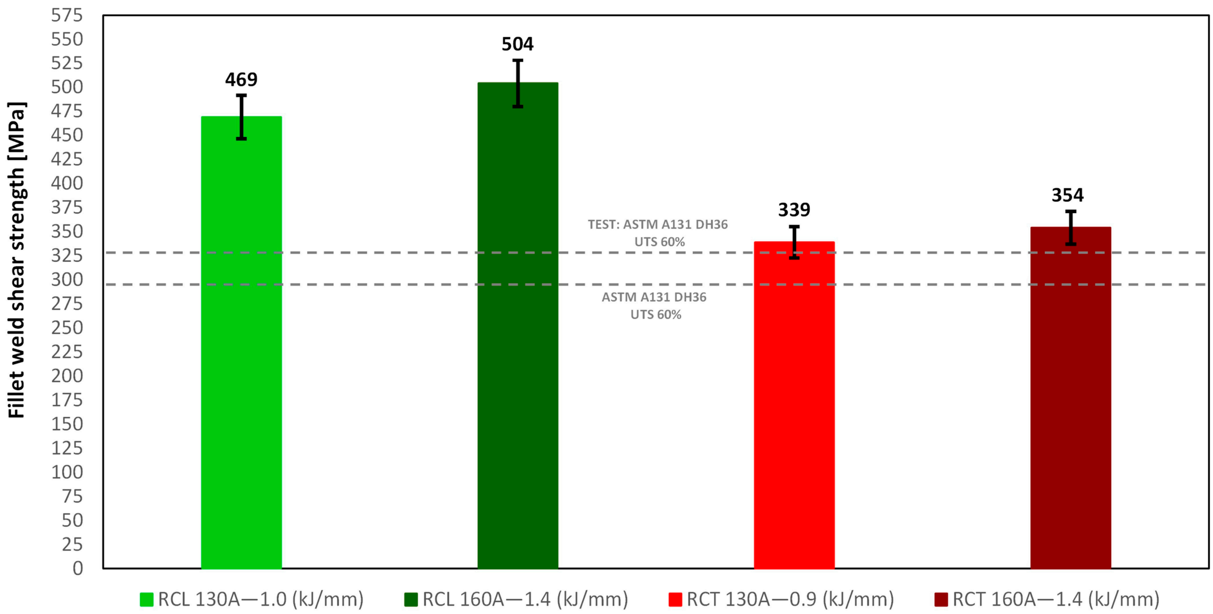

Figure 12. Fillet weld longitudinal (RCL) and transversal (RCT) shear strength tests.

4. Discussion

The microstructures of UWW fillet T welds in the HAZ exhibit a difference between low and high heat inputs, as presented in Figure 7. At low heat inputs, the microstructure mainly consists of polygonal ferrite (PF), upper bainite (UB), and retained austenite (RA) due to the slower cooling rate caused by the low current and second weld bed applied to the joint. On the other hand, even using a dual weld bed at high heat inputs leads to a faster cooling rate and the formation of a microstructure comprising PF and lath-tempered martensite (LTM) because of the higher heat input. Microstructures of fillet weld shear strength display similar results between low and high heat inputs because of the use of a single weld bed producing microstructures composed of lath martensite (LM), PF, acicular ferrite (AF), and UB, RA, and prior austenite grain boundaries (PAGB). To achieve uniform microstructures, using a high heat input single weld bed at a slow and constant welding speed is preferable, resulting in a microstructure of PF and LTM, which produces a non-brittle and uniform weld joint. Thus, the use of a high heat input at slow welding rates is preferred because the resulting microstructure increases the ductility of the welding joint, avoiding brittle behavior, which is consistent with the findings of prior studies on similar materials by Gao Wenbin et al. [25], Gao Wenbin et al. [29], Toumpis Athanasios et al. [37], Li Hongliang et al. [41], Di Xinjie et al. [42], Macias Fernando et al. [38], Kozlowska Aleksandra et al. [43], Meng Fanxia et al. [39], Zhang Hongmei et al. [40], and Min-Seok Baek et al. [48].

Figure 13 displays each heat input's maximum Vickers hardness results. It can be seen that for welded test specimens with 160 A, the maximum Vickers hardness increases as the thermal input decreases. Similarly, the hardness of welded specimens with 130 A increases as the thermal input decreases. Moreover, because the welding speed plays a role in heat input, an increase in welding speed leads to an increase in Vickers hardness for shear strength specimens due to the decrease in heat input causing brittle microstructures. However, this relationship is not maintained for T fillet weld specimens due to the multiple passes used to make the weld, affecting the microstructure and the Vickers hardness.

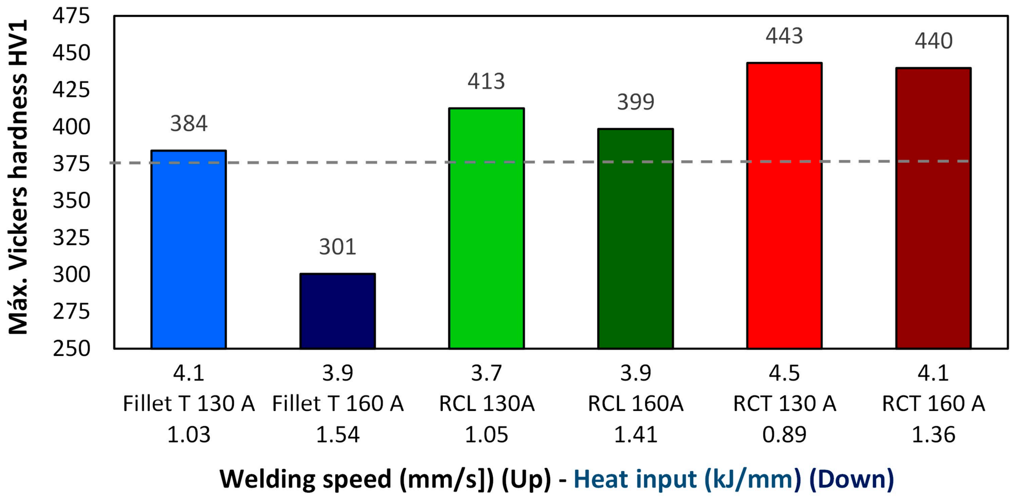

Figure 13. Fillet T, fillet weld longitudinal (RCL) and transversal (RCT) maximum hardness.

Table 10.2 in AWS D3.6 [19] establishes that the maximum Vickers hardness acceptance criteria for B-class welds is 375 HV. For fillet weld shear strength, numeral 10.4.2.2 requires it to be above 60% of the specified minimum tensile strength of the base metal (490 MPa) described in Table 5. This indicates that almost all fillet T, RCL, and RCT welds do not comply with the criteria due to the microstructures, hardnesses, and shear strengths (only for RCL and RCT) presented in the welded joints. However, weld specimens welded with a welding speed of 3.9 mm/s and a heat input of 1.4 kJ/mm present the closest achievement of the criteria because the Vickers hardness is 5.7% above the criteria and the fillet weld shear strength is about 3% above the criteria. Shear strength test results displayed in Figure 12 indicate that welding parameters for the RCL and RCT shown in Table 3 can achieve the minimum acceptable criteria for the fillet weld shear strength described in AWS D3.6.

5. Conclusions

This study aimed to assess the effect of welding heat input on the weldability of underwater wet-welded ASTM A131 DH36 fillet joints. The following conclusions can be drawn based on the findings:

- Fillet weld test specimens (fillet T, RCL, and RCT) with higher heat inputs ranging from 1.4 kJ/mm to 1.5 kJ/mm, using currents around 160 A, voltages of approximately 30 V, and welding speeds of about 4.0 mm/s, demonstrated better weldability compared to those welded with lower heat inputs between 0.9 kJ/mm and 1.0 kJ/mm, using currents around 130 A with similar voltages and welding speeds. High heat input fillet weld shear strength specimens were closer to meeting the acceptance criteria specified in AWS D3.6 for hardness, macroetch, and shear strength, indicating their suitability for underwater wet welding fillet joint applications. However, fillet T welds exhibited poorer performance due to the presence of multiple welding defects. The non-compliance of almost all fillet T, RCL, and RCT welds with the acceptance criteria, as outlined in AWS D3.6, can be attributed to the microstructures, hardnesses, and shear strengths observed in the welded joints. Notably, Table 10.2 in AWS D3.6 establishes a maximum Vickers hardness acceptance criterion of 375 HV for B-class welds, while numeral 10.4.2.2 requires the fillet weld shear strength to exceed 60% of the specified minimum tensile strength of the base metal (490 MPa) described in Table 5. However, weld test specimens welded with a welding speed of 3.9 mm/s and a heat input of 1.4 kJ/mm demonstrated the closest achievement of the acceptance criteria. These welds exhibited a Vickers hardness that surpassed the criteria by 5.7% and a fillet weld shear strength that exceeded the criteria by approximately 3%. The test results align with those reported by Gao Wenbin et al. [29] who found similar hardness, maximum tensile strength, and elongation in joints welded with a heat input of 1.4 kJ/mm. Additionally, the shear strength test results, as shown in Figure 12, indicated that the welding parameters for the RCL and RCT specimens presented in Table 3 have the potential to meet the minimum acceptable criteria for the fillet weld shear strength specified in AWS D3.6.

- The fillet break test conducted on fillet T specimens revealed that higher heat input welds exhibited superior weld soundness with fewer critical welding defects compared to the lower heat input specimens in underwater welding applications. This improvement can be attributed to the increased penetration of the weld metal into the joint, resulting in a significant reduction in critical defects, such as incomplete penetration (IP) and lack of fusion (LF). It is important to note that the presence of these defects is deemed unacceptable according to the acceptance criteria outlined in AWS D3.6, regardless of the heat input level. Although fillet break tests could not be conducted on the RCL and RCT test specimens due to their joint configuration, it is reasonable to infer that similar behavior may be observed in their respective weld beads. This inference is supported by the study conducted by Amirafshari P. et al. [34], whose test results align with the notion that 90 percent of welding defects occur in fillet joints, while 10 percent are found in butt weld joints. However, it is crucial to note that the number of defects in a weld is not solely determined by a single variable; it also depends on other factors, such as the skill level of the welder. The microstructural analysis of fillet T joints and longitudinal and transversal shear strength joints welded with high and low heat inputs did not reveal significant differences between the microstructures produced by each heat input when observed by optical and scanning electron microscopy. However, a notable difference was observed in fillet T joints compared to fillet weld shear strength joints due to the use of multiple welding passes in fillet T joints, resulting in a slower cooling rate that significantly changes the microstructure of the joint. This slower cooling rate also affects the hardness of the joints. It is recommended to utilize a single weld bead with high heat input to achieve uniform microstructures. Using a high heat input at a slow and constant welding speed produces a microstructure of polygonal ferrite (PF) and lath-tempered martensite (LTM), which increases the strength of the welded joint but can produce a slightly brittle behavior.
- This study on the weldability and mechanical properties of ASTM A131 DH36 fillet weld joints using UWW-SMAW contributes to the advancement of knowledge in the field. It facilitates the development of welding procedures for on-site repairs of naval vessels in marine environments, including challenging conditions such as Antarctica. By ensuring the quality and soundness of welded joints, this research helps mitigate the risks of potential vessel sinking and the resulting environmental consequences. The significance of this study is particularly crucial in the Antarctic scenario, where the harsh environment and complex response capabilities necessitate the adoption of environmentally friendly welding practices. This research addresses the evolving operational requirements of ARC naval vessels and aims to support sustainable scientific expeditions by promoting environmentally friendly welding practices. The obtained methodology, welding parameters, and test results contribute to the establishment of innovative, technological, and scientific research documents that can contribute to the aims established in the Colombian Maritime Interests [49] and the 3990 National Council of Economic and Social Policy (CONPES 3990—Consejo Nacional de Política Económica y Social) [50].

Author Contributions: Conceptualization, H.A.G.R., E.E.N.N., L.P.C.M. and E.A.B.B.; methodology, E.E.N.N. and H.A.G.R.; validation, E.E.N.N., H.A.G.R. and L.P.C.M.; formal analysis, H.A.G.R. and E.E.N.N.; investigation, H.A.G.R. and E.E.N.N.; data curation, H.A.G.R. and E.E.N.N.; writing—original draft preparation, H.A.G.R.; writing—review and editing, H.A.G.R., L.P.C.M. and E.E.N.N.; visualization, H.A.G.R.; supervision, L.P.C.M. and E.A.B.B.; project administration, L.P.C.M. and E.A.B.B.; funding acquisition, E.A.B.B. and L.P.C.M. All authors have read and agreed to the published version of the manuscript.

Funding: This research was funded by the Ministry of Science, Technology, and Innovation of Colombia, Programa Nacional de Ciencia, Tecnología e Innovación en Seguridad y Defensa, Convocatoria 1007-2019 Invitación a presentar propuestas para la ejecución de proyectos ARC 2019, Code 75887.

Data Availability Statement: The data presented in this study are available only upon request from the corresponding author and with authorization from the Colombian Ministry of National Defense.

Acknowledgments: The authors are grateful for the support of the Ministry of Defense of Colombia, Colombian National Navy, Department of Diving and Salvage of the National Navy, Diving and Rescue School of the National Navy, Corporación de Ciencia y Tecnología para el Desarrollo de la Industria Naval Marítima y Fluvial—COTECMAR, Colombo-Alemán Nacional Center—SENA CNCA, Acesco Colombia, and the AC Committee.

Conflicts of Interest: The authors declare no conflict of interest.

References

1. Comisión Colombiana del Oceano CCO, Asuntos Internacionales—Asuntos Antárticos. Available online: https://cco.gov.co/asuntos-antarticos.html (accessed on 20 March 2023).
2. Comisión Colombiana del Oceano CCO, Programa Antártico Colombiano PAC. Available online: https://cco.gov.co/cco/publicaciones/83-publicaciones/137-programa-antartico-colombiano.htm (accessed on 20 March 2023).
3. Armada Nacional de Colombia ARC, Plan Estratégico Naval 2020–2023 PEN. Available online: https://www.armada.mil.co/es/content/i-documento-pen-2020-2023-0 (accessed on 20 March 2023).
4. Zhao, W.; Feng, G.; Zhang, M.; Ren, H.; Sinsabvarodom, C. Effect of low temperature on fatigue crack propagation rates of DH36 steel and its butt Weld. *Ocean. Eng.* **2019**, *196*, 106803. [CrossRef]
5. Tomków, J. Weldability of Underwater Wet-Welded HSLA Steel: Effects of Electrode Hydrophobic Coatings. *Materials* **2021**, *14*, 1364. [CrossRef] [PubMed]
6. Klett, J.; Hecht-Linowitzki, V.; Grünzel, O.; Schmidt, E.; Maier, H.J.; Hassel, T. Effect of the water depth on the hydrogen content in SMAW wet welded joints. *SN Appl. Sci.* **2020**, *2*, 1–14. [CrossRef]
7. Surojo, E.; Gumilang, A.H.; Triyono, T.; Prabowo, A.R.; Budiana, E.P.; Muhayat, N. Effect of Water Flow on Underwater Wet Welded A36 Steel. *Metals* **2021**, *11*, 682. [CrossRef]
8. Vashishtha, P.; Wattal, R.; Pandey, S.; Bhadauria, N. Problems encountered in underwater welding and remedies—A review. *Mater. Today Proc.* **2022**, *64*, 1433–1439. [CrossRef]
9. Pan, J.; Yang, L.; Hu, S.; Chai, S. Numerical analysis of thermal cycle characteristics and prediction of microstructure in multi-pass UWW. *Int. J. Adv. Manuf. Technol.* **2016**, *84*, 1095–1102. [CrossRef]
10. Fydrych, D.; Rogalski, G.; Labanowski, J. Weldability of high strength steel in underwater environment. *Weld. Int.* **2016**, *30*, 175–181. [CrossRef]
11. Colak, Z.; Ayan, Y.; Kahraman, N. Weld morphology and mechanical performance of marine structural steel welded underwater in a real marine environment. *Int. J. Adv. Manuf. Technol.* **2020**, *109*, 491–501. [CrossRef]
12. Winarto, W.; Purnama, D.; Churniawan, I. The effect of different rutile electrodes on mechanical properties of underwater wet welded AH-36 steel plates. *AIP Conf. Proc.* **2018**, *1945*, 020048.
13. Yang, L. Microstructure and mechanical properties of FCTIG-welded DH36 steel with rutile-type and basic-type flux cored wires. *J. Mater. Process. Technol.* **2019**, *275*, 116363. [CrossRef]
14. Yasari, N.M.L.P.K.; Muhayat, N.; Triyono, T.; Saputro, Y.C.N. Microstructural and Mechanical Properties of Underwater Wet Welded SS400 Steel. *J. Mech. Eng.* **2018**, *3*, 168–179.
15. Lu, H.; Dong, P.; Boppudi, S. Strength analysis of fillet welds under longitudinal and transverse shear conditions. *Mar. Struct.* **2015**, *43*, 87–106. [CrossRef]
16. *ASTM A131/A131M-19*; Standard Specification for Structural Steel for Ships. ASTM International: West Conshohocken, PA, USA, 2019. [CrossRef]
17. *ASTM E415-21*; Standard Test Method for Analysis of Carbon and Low-Alloy Steel by Spark Atomic Emission Spectrometry. ASTM International: West Conshohocken, PA, USA, 2021. [CrossRef]
18. *ASTM E8-22*; Standard Test Methods for Tension Testing of Metallic Materials. ASTM International: West Conshohocken, PA, USA, 2022. [CrossRef]
19. *AWS D3.6M:2017*; Underwater Welding Code. AWS American Welding Society: Danvers, MA, USA, 2017; ISBN 978-0-87171-902-7.

20. *AWS B4.0:2016*; Standard Methods for the Mechanical Testing of Welds. AWS American Welding Society: Danvers, MA, USA, 2016; ISBN 978-0-87171-889-1.
21. *ASTM E384-22*; Standard Test Method for Microindentation Hardness of Materials. ASTM International: West Conshohocken, PA, USA, 2022. [CrossRef]
22. *ASTM E3-11(2017)*; Standard Guide for Preparation of Metallographic Specimens. ASTM International: West Conshohocken, PA, USA, 2017. [CrossRef]
23. *ASTM E407-07(2015)e1*; Standard Practice for Microetching Metals and Alloys. ASTM International: West Conshohocken, PA, USA, 2015. [CrossRef]
24. *ASTM E340-15*; Standard Practice for Macroetching Metals and Alloys. ASTM International: West Conshohocken, PA, USA, 2015. [CrossRef]
25. Gao, W.; Wang, D.; Cheng, F.; Di, X.; Deng, C.; Xu, W. Microstructural and mechanical performance of underwater wet welded S355 steel. *J. Mater. Process. Technol.* **2016**, *238*, 333–340. [CrossRef]
26. Tomków, J.; Rogalski, G.; Fydrych, D.; Łabanowski, J. Advantages of the Application of the Temper Bead Welding Technique During Wet Welding. *Materials* **2019**, *12*, 915. [CrossRef]
27. Tomków, J.; Fydrych, D.; Rogalski, G. Dissimilar underwater wet welding of HSLA steels. *Int. J. Adv. Manuf. Technol.* **2020**, *109*, 717–725. [CrossRef]
28. Bechetti, D.H.; Semple, J.K.; Zhang, W.; Fisher, C.R. Temperature-Dependent Material Property Databases for Marine Steels—Part 1: DH36. *Integr. Mater. Manuf. Innov.* **2020**, *9*, 257–286. [CrossRef]
29. Gao, W.B.; Wang, D.P.; Cheng, F.J.; Deng, C.Y.; Xu, W. Underwater Wet Welding for HSLA Steels: Chemical Composition, Defects, Microstructures, and Mechanical Properties. *Acta Metall. Sin.* **2015**, *28*, 1097–1108. [CrossRef]
30. Rasband, W.S.; ImageJ, U.S. National Institutes of Health, Bethesda, Maryland, USA, 1997–2018. Available online: https://imagej.nih.gov/ij/ (accessed on 29 May 2023).
31. Zambrano, O.A.; Gómez, J.A.; Coronado, J.J.; Rodríguez, S.A. The sliding wear behaviour of steels with the same hardness. *Wear* **2019**, *418–419*, 201–207. [CrossRef]
32. Queiros, G.W.; García, L.; de la Fuente, T.; de Salazar, J.M.G.; Criado, A.J. Metallographic Interpretation of the Morphology of the Very Old Pearlite. *Arch. Phys. Res.* **2019**, *10*, 42–51.
33. Civjan, S.; Guihan, T.; Peterman, K. Testing of oxyacetylene weld strength. *J. Constr. Steel Res.* **2020**, *168*, 105921. [CrossRef]
34. Amirafshari, P.; Barltrop, N.; Wright, M.; Kolios, A. Weld defect frequency, size statistics and probabilistic models for ship structures. *Int. J. Fatigue* **2021**, *145*, 106069. [CrossRef]
35. Santos, V.R.; Bracarense, A.Q.; Pessoa, E.C.P.; Marinho, R.R.; Rizzo, F.C.; Junior, R.C.; Monteiro, M.J. Development of oxyrutile low alloy ferritic electrode for wet welding. *J. Mater. Res. Technol.* **2022**, *21*, 1223–1247. [CrossRef]
36. Barzegar-Mohammadi, S.; Haghpanahi, M.; Zeinoddini, M.; Miresmaeili, R. Cooling rate effects on fatigue life prediction using hardness measurements for in-service steel patch-welds with and without TIG dressing treatment. *Structures* **2023**, *50*, 1285–1302. [CrossRef]
37. Toumpis, A.; Galloway, A.; Cater, S.; McPherson, N. Development of a process envelope for friction stir welding of DH36 steel—A step change. *Mater. Des.* **2014**, *62*, 64–75. [CrossRef]
38. López, F.M.; Vidaurri, L.E.R.; Dávila, J.L.A.; Hdz-García, H.M.; Hernández-Rodríguez, A.; Mondragon, J.J.R. Effect of depth on the weldability of ferritic steels in simulated environments joined by wet welding. *Weld. Int.* **2018**, *32*, 561–569. [CrossRef]
39. Meng, F.; Tian, Y.; Ye, Q.; Wang, Z.; Wu, D. Effect of Rolling and Heat Treatment Process Tempering on the Microstructure and Mechanical Performance of Cr–Ni–Mo High-Strength Ship Steel. *Steel Res. Int.* **2021**, *92*, 2100106. [CrossRef]
40. Zhang, H.; Huo, M.; Ma, Z.; Wu, H.; Su, G.; Li, L.; Zhang, T.; Lin, F.; Chen, F.; Jiang, Z. Effects of Quenching and Tempering Heat Treatment Processing on the Microstructure and Properties of High-Strength Hull Steel. *Metals* **2022**, *12*, 914. [CrossRef]
41. Li, H.; Liu, D.; Ma, Q.; Guo, N.; Song, X.; Feng, J. Microstructure and mechanical properties of dissimilar welds between 16Mn and 304L in underwater wet welding. *Sci. Technol. Weld. Join.* **2019**, *24*, 1–7. [CrossRef]
42. Di, X.; Ji, S.; Cheng, F.; Wang, D.; Cao, J. Effect of cooling rate on microstructure, inclusions and mechanical properties of weld metal in simulated local dry underwater welding. *Mater. Des.* **2015**, *88*, 505–513. [CrossRef]
43. Kozłowska, A.; Grajcar, A.; Janik, A.; Radwański, K.; Krupp, U.; Matus, K.; Morawiec, M. Mechanical and thermal stability of retained austenite in plastically deformed bainite-based TRIP-aided medium-Mn steels. *Arch. Civ. Mech. Eng.* **2021**, *21*, 133. [CrossRef]
44. Jia, N.; Shen, Y.F.; Liang, J.W.; Feng, X.W.; Wang, H.B.; Misra, R.D.K. Nanoscale spheroidized cementite induced ultrahigh strength-ductility combination in innovatively processed ultrafine-grained low alloy medium-carbon steel. *Sci. Rep.* **2017**, *7*, 2679. [CrossRef] [PubMed]
45. Medina, G.P.; Ferreira, H.L.; Robledo, P.Z.; Pérez, A.M.; Valdés, F.A.R. Microstructural Development in a TRIP-780 Steel Joined by Friction Stir Welding (FSW): Quantitative Evaluations and Comparisons with EBSD Predictions. *Soldagem Inspeção* **2016**, *21*, 146–155. [CrossRef]
46. Kalyankar, V.; Chudasama, G. Effect of post weld heat treatment on mechanical properties of pressure vessel steels. *Mater. Today Proc.* **2018**, *5*, 24675–24684. [CrossRef]
47. Zhao, W.; Feng, G.; Liu, W.; Ren, H. Research on Fatigue Properties of Typical Welded Joints of DH36 Steel at −60 °C. *Appl. Sci.* **2020**, *10*, 3742. [CrossRef]

48. Baek, M.; Kim, K.; Park, T. Quantitative phase analysis of martensite-bainite steel using EBSD and its microstructure, tensile and high-cycle fatigue behaviors. *Mater. Sci. Eng. A* **2020**, *785*, 139375. [CrossRef]
49. Comisión Colombiana del Oceano CCO, Publicaciones—Intereses Marítimos Colombianos. Available online: https://cco.gov.co/cco/publicaciones/83-publicaciones/881-intereses-maritimos-de-colombia.html (accessed on 25 June 2023).
50. Departamento Nacional de Planeación de Colombia, Consejo Nacional de Política Económica y Social CONPES 3990. Available online: https://cco.gov.co/cco/publicaciones/83-publicaciones/794-conpes-colombia-potencia-bioceanica-sostenible.html (accessed on 25 June 2023).